

Sample cells for probing solid/liquid interfaces with broadband sum-frequency-generation spectroscopy

Dominique Verreault, Volker Kurz, Caitlin Howell, and Patrick Koelsch^{a)}

Department of Applied Physical Chemistry, University of Heidelberg, Im Neuenheimer Feld 253, D-69120 Heidelberg, Germany and Institute of Toxicology and Genetics (ITG), Karlsruhe Institute of Technology, Campus North, Hermann-von-Helmholtz-Platz 1, D-76344 Eggenstein-Leopoldshafen, Germany

(Received 17 February 2010; accepted 11 May 2010; published online 24 June 2010)

Two sample cells designed specifically for sum-frequency-generation (SFG) measurements at the solid/liquid interface were developed: one thin-layer analysis cell allowing measurement of films on reflective metallic surfaces through a micrometer layer of solution and one spectroelectrochemical cell allowing investigation of processes at the indium tin oxide/solution interface. Both sample cells are described in detail and data illustrating the capabilities of each are shown. To further improve measurements at solid/liquid interfaces, the broadband SFG system was modified to include a reference beam which can be measured simultaneously with the sample signal, permitting background correction of SFG spectra in real time. Sensitivity tests of this system yielded a signal-to-noise ratio of 100 at a surface coverage of 0.2 molecules/nm². Details on data analysis routines, pulse shaping methods of the visible beam, as well as the design of a purging chamber and sample stage setup are presented. These descriptions will be useful to those planning to set up a SFG spectrometer or seeking to optimize their own SFG systems for measurements of solid/liquid interfaces. © 2010 American Institute of Physics. [doi:10.1063/1.3443096]

I. INTRODUCTION

The investigation of molecular behavior at solid interfaces *in situ* is of significant interest in the field of surface science, particularly in such issues as the development of biocompatible materials and material coatings, as well as a furthering of the knowledge of basic surface chemistry and physics.¹⁻⁴ Recently, the technique of sum-frequency-generation (SFG) spectroscopy has emerged as a tool particularly well suited to this task due to its surface sensitivity, molecular-level detection, and ability to function under standard conditions.⁵⁻⁷ SFG spectroscopy has been previously applied to the investigation of various materials at the gas/solid interface,⁸ the gas/liquid interface,⁹⁻¹¹ and the liquid/liquid interface.^{12,13} However, applications of this technique to solid/liquid interfaces have been fewer in number¹⁴ due at least in part to the difficulties associated with the more complex sample stage geometry required.

The first approaches to overcoming these difficulties consisted of probing the solid/liquid interface in setup where the solid itself was a flat window of optically transparent material.¹⁵⁻¹⁹ This approach has yielded valuable information about the adsorption of polyelectrolyte solutions,¹⁵ the behavior of water at the α -quartz interface at various pH values,¹⁶ the conformation of liquid poly(ethylene glycol) in contact with solid polymers,¹⁷ and the adsorption of amino acids at hydrophobic and hydrophilic interfaces.¹⁸ However, as the focus of these studies was on the outcome of the experiments rather than the measurement method, the descriptions of the sample cells used were somewhat limited.

Recent measurements made by York *et al.* at the polystyrene/air interface demonstrated that signal strength in SFG spectra was enhanced when the incoming beams were directed through a prism instead of a flat window. This enhancement in the SFG signal is usually found by having one of the incident beams near the total internal reflection (TIR) condition.²⁰ However, it was also shown that the SFG intensity is strongly influenced by the dispersion of the absorptive medium and that care must be taken in the quantitative analysis of the SFG experimental data.²¹ Nevertheless, the former geometry had been previously used by Becraft and Richmond²² in their SFG investigations of water orientation at the CaF₂/H₂O interface, as well as by Hayes *et al.*²³ in their second-harmonic-generation studies of metal cations at the fused quartz/H₂O interface.

However, all of the methods used in the above-mentioned studies require that the solid surface be both visible (VIS) and IR transparent. Furthermore, when investigating thin films, it is necessary that the molecules of interest be immobilizable on this transparent surface, which is not the situation in many interesting phenomena at the solid/liquid interface. Stein *et al.*²⁴ worked to overcome this limitation by probing through the backside of a fused silica window coated with a 20 nm layer of gold and covered with self-assembled monolayers (SAMs) of alkanethiols or ethylene glycols. Using this setup, they were able to successfully quantify the percentage of water retained in these films. However, previous works characterizing the synthesis of very thin metal films have shown that achieving a fully closed film of such thickness is no trivial task,^{25,26} and that surface roughness stemming from incomplete film formation can complicate the interpretation of the obtained SFG spectra.²⁵ Further-

^{a)} Author to whom correspondence should be addressed. Electronic mail: patrick.koelsch@kit.edu.

more, using thin metal films increases the risk of total film ablation if the intensity of the incoming beams is not carefully monitored and controlled. In this work we present a thin-layer analysis (TLA) cell which solves the problems of being limited to transparent substrates or very thin metal films, offering the ability to probe the solid/liquid interface on any opaque and suitably reflective substrate.

In addition to the TLA cell, we introduce a new spectro-electrochemical (SPEC) cell specially designed to perform *in situ* SFG measurements in a potentiostatically controlled electrochemical environment. Numerous interesting processes occurring at the solid/liquid interface involve charging effects. Nevertheless, to date there has been much less work done using both SFG and electrochemistry at these interfaces.²⁷ The majority of studies have been mostly concerned with charged noble metals electrodes (Ag, Au, and Pt) and their effects on CO (Refs. 28–31) and cyanide/thiocyanate ion adsorption,^{32–36} on water orientation,^{37–41} or on the conformation and self-assembly of alkanethiols monolayers.^{42–44} These studies have mainly relied on SPEC cells based on earlier designs developed for IR spectroscopy,⁴⁵ where a thin layer of electrolyte (1–5 μm) is trapped between an electrode and an IR-transparent material, usually a disk- or prismatic-shaped CaF_2 window. However, these devices can either introduce an additional angular parameter in the calculation of the SFG beam output angle or reduce signal-to-noise ratio (SNR) in many spectral regions. Moreover, such cells do not allow measurements adjacent to a bulk aqueous environment and under varying flow conditions. Recently, new cell designs circumventing these limitations have appeared, although details on their construction were limited.^{46,47} Our SPEC cell is based on the deposition of a VIS- and IR-transparent indium tin oxide (ITO) conductive layer directly on the basal face of a hemicylindrical-shaped CaF_2 prism. The use of an ITO layer makes it possible to probe charging effects such as ion condensation or water orientation in electric fields, while the prism shape alleviates any angular constraints or signal attenuation problems.

The sample cells and instrumental details included in this work represent, to the best of our knowledge, the first such thorough descriptions for SFG at the solid/liquid interface, and the schematics and applications described herein will provide a reference for those wishing to either begin or optimize their own *in situ* SFG measurements.

II. EXPERIMENTAL SETUP

A. SFG spectrometer

The generation of nonlinear signals from interfacial molecules requires high intensity laser light sources. Therefore, picosecond and femtosecond laser setups are most often used in SFG spectroscopy.⁴⁸ Picosecond-based systems usually have a large scanning range ($\sim 1000\text{ cm}^{-1}$) with a spectral acquisition time on the order of tens of minutes. A picosecond-based laser system is tuned within a certain frequency range and an SFG signal is recorded by integrating the intensity at each frequency. Broadband SFG spectrometers based on femtosecond tunable laser systems are con-

ceptually different. In these, the broad SFG signal is imaged through a spectrometer. This setup allows the detection of SFG signals in a narrower spectral range ($\sim 70\text{--}200\text{ cm}^{-1}$) with temporal resolution usually on the order of seconds. The sample cells presented in Sec. II F can be used for both picosecond and femtosecond SFG spectrometers. Dynamic processes on time scales from seconds to minutes are accessible to both type of systems. However, kinetic measurements obtained by picosecond systems are restricted to one fixed frequency,⁴⁹ while femtosecond systems can record a spectral range.

Our femtosecond SFG spectrometer setup is based on a broad bandwidth scheme.⁵⁰ It consists of a femtosecond regenerative amplifier (RGA) (Spitfire Pro 35F XP, Spectra-Physics; sub-35 fs, 1 kHz) seeded by a mode-locked Ti:sapphire oscillator (Tsunami 3941-MS, Spectra-Physics; sub-30 fs, 80 MHz) with a tunable wavelength centered at 800 nm. The regenerative amplifier and seed laser are pumped by frequency-doubled *Q*-switched neodymium-doped yttrium lithium fluoride (Nd:YLF) (Empower 30, Spectra-Physics; 30 W, 1 kHz, 527 nm) and Nd:YVO₄ (Millenia Pro 5s, Spectra-Physics; 5 W, 532 nm) solid-state lasers, respectively. The RGA generates 120 fs duration pulses centered at 800 nm with a repetition rate of 1 kHz and an average power of 4 W. The amplified output beam is then split up and the larger fraction (80%) is used to pump an automated optical parametric amplifier (OPA) (TOPAS-C, Light Conversion) coupled to a noncollinear difference-frequency generator (NDFG) (Light Conversion). This generates broadband (FWHM $\sim 70\text{--}200\text{ cm}^{-1}$) IR pulses which can be tuned from 2.6 to 12 μm . The signal and idler beams are spatially separated and spectrally filtered by a Ge plate (Crystec). The remaining fraction of the output beam (20%) is fed into an air-spaced Fabry-Pérot etalon (SLS Optics; spacing $d = 12.5\text{ }\mu\text{m}$, free spectral range FSR = 398.29 cm^{-1} , effective finesse $F_{\text{eff}} = 57.48$ at 790 nm) which gives narrowband (FWHM $\sim 1\text{ nm}$), asymmetric picosecond VIS pulses (see Sec. II A 1). A broadband reference (REF) beam is generated simultaneously by sum frequency mixing of small portions of the IR ($\sim 1\%$) and VIS ($\sim 1\%$) beams in one of the following nonlinear crystals: 0.6 mm thick LiIO_3 (2.7–5 μm , $\theta = 21.4^\circ$, and $\phi = 0^\circ$), 0.2 mm thick AgGaS_2 (5–6 μm , $\theta = 71^\circ$, and $\phi = 45^\circ$), or AgGaS_2 (6–10 μm , $\theta = 54.4^\circ$, and $\phi = 45^\circ$) (TOPAG Lasertechnik). The beam path length prior to the LiIO_3 crystal is the same as the beam path length to the sample stage. This allows for the recording of the exact spectral profile of the incident IR beam on the sample stage which can then be used for the data analysis as described in Sec. II D. Linearly polarized IR, REF, and VIS beams are independently directed and focused on the sample surface with incident angles (relative to the surface normal) of 60° , 68° , and 70° , respectively (Fig. 1).

A broadband SFG beam is produced when the narrowband VIS and broadband IR beams are spatially and temporally overlapped at the sample surface within a spot of $\sim 200\text{ }\mu\text{m}$ in diameter. Figure 2 shows the beam profile of the VIS pulse at the sample. The elliptical shape is due to the incoming angle. The temporal overlap is accomplished through the use of motorized delay lines. The incidence

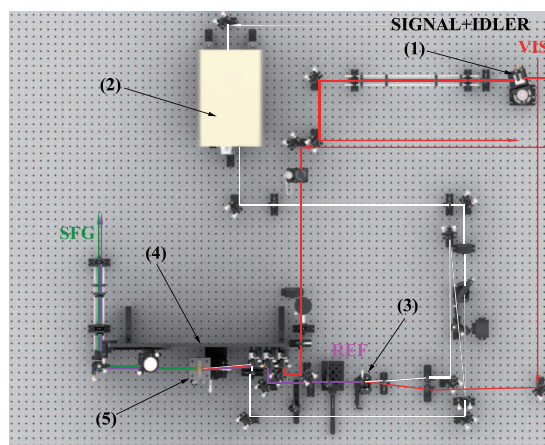


FIG. 1. (Color) Top view image of the optical layout of the broadband SFG system after the OPA. The labels denote (1) Fabry–Pérot etalon, (2) NDFG, (3) nonlinear crystal for the reference line, (4) vertical breadboard, and (5) sample stage. The IR, REF, SFG, and VIS beams are represented by white, purple, green, and red solid lines, respectively.

angle of the REF beam is carefully adjusted so that on reflection it propagates collinearly with the SFG beam. Maximum energies of $\sim 30 \mu\text{J}/\text{pulse}$ for the IR beam and $\sim 40 \mu\text{J}/\text{pulse}$ for the VIS beam can be obtained immediately before the sample. Usually, the energy of the incoming beams is adjusted by pinholes to prevent bubble formation or sample ablation. The intensity of the reflected REF beam is matched to that of the SFG beam using a variable neutral density filter prior to the sample. The outgoing SFG and REF beams are collimated by lenses, filtered through a short-pass filter (3rd Millennium 770SP, Laser Components), and dispersed in an imaging spectrograph (Shamrock SR-301i-B, Andor Technology; focal length $f=303 \text{ mm}$, 1200 grooves/mm grating blazed at 500 nm) equipped with both a photomultiplier (R9110, Hamamatsu) and an air-cooled, back-illuminated high-resolution charge-coupled device (CCD) camera (iDus DU420A-BR-DD, Andor Technology; 254×1024 pixels). SFG spectra with reasonable SNR are typically obtained on a time scale of microseconds to seconds. For alignment purposes, spectra can be recorded within one or two pulses, allowing real-time intensity optimization and frequency adjustment. Spectra are usually taken with a *ppp* polarization combination for the SFG, VIS, and IR beams, respectively. Other polarization combinations (*ssp*, *sps*, and *pss*) are also accessible by rotation of the IR and VIS beams through the use of half-wave plates and/or a periscope.

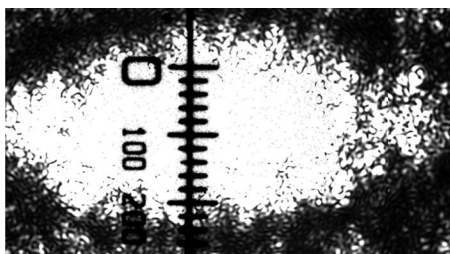


FIG. 2. Beam profile of the VIS pulse at the sample stage. The scale shown is in micrometer units. This image was acquired using a microscope mounted above the sample stage.

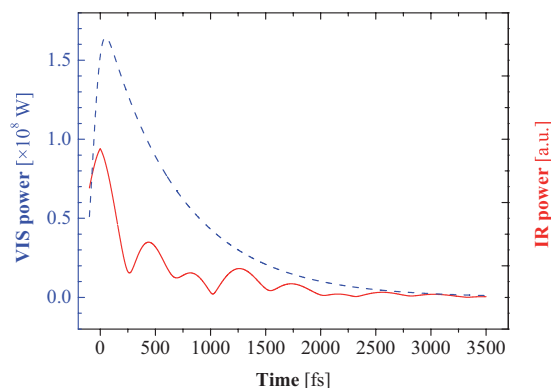


FIG. 3. (Color) Time profile of VIS pulse (dashed line) and molecular vibrations of typical CH stretches (solid line).

1. Pulse shaping

The spectral resolution of the SFG signal depends on the temporal pulse width of the VIS beam. To illustrate these dependencies, Fig. 3 shows a calculation of the time profile of the VIS beam (dashed line) and the resulting time profile of three typical molecular vibrations (solid line). The time profile of the molecular vibrations exceeds several picoseconds; therefore the duration of the VIS pulse needs to be on the same order to resolve these vibrations into an SFG spectrum in the frequency domain. This pulse duration can be achieved by directing the VIS beam through a Fabry–Pérot etalon to obtain a prolonged asymmetric time profile. For the calculation of the corresponding VIS time profile after the pulse shaper, the specifications of the etalon described in the Sec. II A were used. The cavity lifetime τ is determined by

$$\tau = \frac{1}{\pi \text{FSR}}. \quad (1)$$

To obtain an approximation of the transmitted intensity, the incoming Gaussian-shaped beam was convoluted with an exponential decay function having a time constant given by the cavity lifetime τ (Ref. 51)

$$I_{\text{VIS,out}}(t) \approx I_{\text{VIS,in}}(t) * e^{-t/\tau} \Theta(t), \quad (2)$$

where $I_{\text{VIS,in}}$ and $I_{\text{VIS,out}}$ are the time-dependent intensities of the VIS beam before and after the etalon, respectively. Since there is no intensity in the cavity before the pulse reaches the etalon, Eq. (2) was weighted with the Heaviside function $\Theta(t)$. To calculate the time profile representing the polarization fields in the frequency domain three Lorentzian oscillators χ_i with equal intensities and widths of 20 cm^{-1} at 2880, 2925, and 2945 cm^{-1} were used (solid line in Fig. 3). Finally, the sum of these three oscillators was Fourier transformed (FT) into the time domain and the intensity is given by

$$I(t) = |\mathcal{F}^{-1}(\chi_i(\omega_i))|. \quad (3)$$

B. Purging chamber

In order to prevent IR beam absorption by ambient gaseous H_2O and CO_2 , the SFG spectrometer setup is supplemented with a home-built purging chamber (Fig. 4). This air-proof chamber covers the optical path of the IR beam

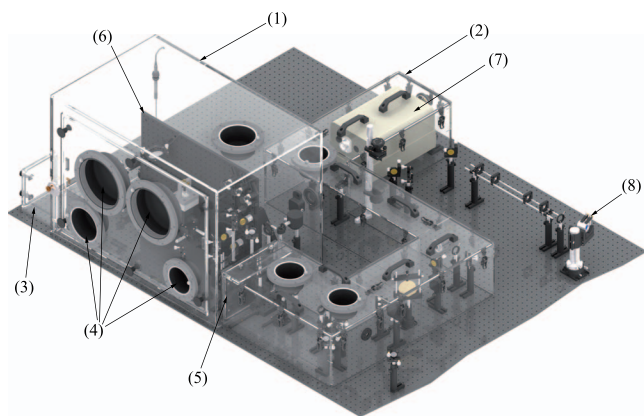


FIG. 4. (Color) Image (isometric view) of the purging chamber. The labels denote (1) main chamber, (2) channel, (3) transfer chamber, (4) Neoprene® gloves, (5) vertical lockable flapping door, (6) breadboard, (7) NDFG, and (8) Fabry-Pérot etalon.

from the NDFG module to the spectrograph. The enclosure is made entirely of acrylic glass and is divided in two sections: a four-compartment channel (volume $V \approx 0.14 \text{ m}^3$) that stretches between the NDFG and the sample stage, and a main chamber ($V \approx 0.30 \text{ m}^3$) that completely surrounds the sample stage. The channel and the chamber have built-in thin optical BaF_2 and BK7 windows (Laser Components) mounted in Teflon holders to allow entrance of OPA (signal and idler) and VIS beams, respectively. The main chamber is supplemented by a small side chamber with a lockable vertical panel permitting sample transfer without disrupting the air purge. Both channel and chamber are air-dried ($\leq 1\%$ RH) by a FTIR purging gas generator (75–45–12VDC, Parker-Balston; 14 l/min) coupled to two additional coalescing prefilters to remove air particulates and hydrocarbon residues. The humidity and temperature in the chamber are monitored by a thermohygrometer (Hytelog-USB, Hygro-sens) mounted on the top panel. When the chamber is not purged, the optical components in the channel can be accessed through removable covers, while those in the chamber can be reached by removal of the front panel. The channel and chamber can be separated from each other by a vertical lockable flapping door, keeping one compartment purged while the other is open. When the purging chamber is in operation, the mirrors important for beam alignment in the channel and the chamber can be reached externally by small Neoprene® gloves. The entire sample holder area (including the transfer chamber) can be accessed via two pairs of ambidextrous, fully rotatable Neoprene® gloves fixed directly to the front panel. All other components necessary to adjust IR and REF beam intensity (e.g., Ge plate, reference crystal, and variable density filter) are motorized and remotely controlled. Two independent side panels, one on the channel and one on the chamber, provide the necessary entry ports for liquid tubes as well as for various electrical cables.

C. Sample stage

The sample stage is comprised of a set of input lenses and mirrors (Laser Components), a multiaxial sample holder, and a set of output mirrors (Fig. 5). All these components are constrained to the same plane of incidence by being fixed

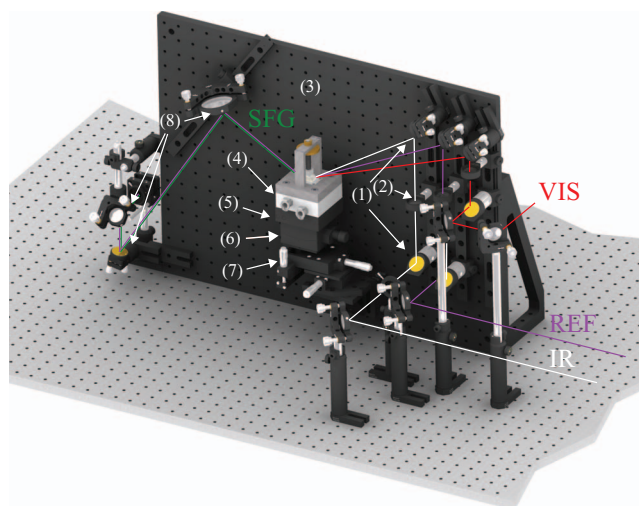


FIG. 5. (Color) Image (isometric view) of the sample stage area (purging chamber not shown). The labels denote (1) input mirrors, (2) input lenses, (3) breadboard, (4) measuring cell, (5) kinematic plates, (6) one-axis goniometer, (7) three-axis rolling block, and (8) output mirrors. The IR, REF, SFG, and VIS beams are represented by white, purple, green, and red solid lines, respectively. The reflected IR and VIS beams are not shown for clarity. The SFG and REF beams after the sample stage are collinear.

directly on an aluminum breadboard (M4560, Thorlabs) positioned vertically on the optical table. Each input beam path consists of a lower mirror/intermediate lens/upper mirror series mounted independently on its own flexible rail system. CaF_2 (or BaF_2) lenses are used for the IR and REF beams, and BK7 lens for the VIS beam (Laser Components), respectively. The sample holder is made of a three-axis (xyz) rolling block with manual micrometric drives (RB13M/M, Thorlabs; 13 mm travel) coupled to a one-axis (θ) manual goniometer (GO90, Owis; $\pm 15^\circ$ rotation). The rotation axis of the goniometer is coincident with the sample surface. A pair of magnetically coupled kinematic plates is then used to dock the measuring cells. A bottom base plate is fastened directly on top of the goniometer, while the top mounting plate is fixed to the base of the measuring cell. This system permits a quick exchange of measuring cells while the position and orientation of the probing plane are preserved. The output beam path is made of a series of three mirrors. The first mirror is larger and acts as a collector for the REF, SFG, and VIS beams. It is mounted on an independent rail system that enables the operator to follow the displacement of the beams induced by the goniometer tilting. The two last mirrors guide the REF and SFG beams to the entrance slit of the spectrograph.

D. Data analysis

The second-order nonlinear polarization $\mathbf{P}^{(2)}$ is given by

$$\mathbf{P}^{(2)} = \varepsilon_0 \chi^{(2)} : \mathbf{E}_{\text{IR}} \mathbf{E}_{\text{VIS}}, \quad (4)$$

where ε_0 is the vacuum permittivity ($8.854 \times 10^{-12} \text{ C/V m}$), $\chi^{(2)}$ is the second-order nonlinear susceptibility, a third rank tensor, and \mathbf{E}_{IR} and \mathbf{E}_{VIS} are the incoming electric fields of the IR and VIS beams, respectively.

The intensity of the SFG signal I_{SFG} is related to the IR (I_{IR}) and the VIS (I_{VIS}) intensities by the relation

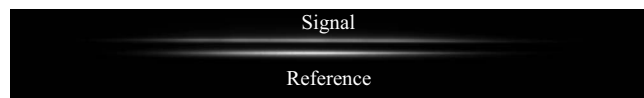


FIG. 6. CCD image of the SFG signals from a Au sample and the reference line.

$$I_{\text{SFG}} \propto |\mathbf{P}^{(2)}|^2 \propto |\chi^{(2)}|^2 I_{\text{IR}} I_{\text{VIS}}. \quad (5)$$

In Eq. (5), $\chi^{(2)}$ consists of two different contributions: one from the substrate (nonresonant) and one from the adsorbate (resonant)⁵²

$$\chi^{(2)} = \chi_{\text{NR}}^{(2)} + \chi_{\text{R}}^{(2)} = \chi_{\text{NR}}^{(2)} + \sum_k \left| \frac{A_k}{(\omega_{\text{IR}} - \omega_k) + i\Gamma_k} \right| e^{i\phi_k}, \quad (6)$$

where the nonresonant contribution $\chi_{\text{NR}}^{(2)}$ is generated by electronic interband transitions occurring within metal substrates.⁵³ The resonant contribution $\chi_{\text{R}}^{(2)}$ is generated from molecular vibrations and modeled as a sum of Lorentzian oscillators with amplitude A_k , resonance frequency ω_k , line-width Γ_k , and phase difference ϕ_k relative to the nonresonant contribution.

The spectral data are fitted by Eq. (5) using a Gaussian shape for the nonresonant signal (reflecting the femtosecond IR profile) and Lorentzian oscillators for the resonant contributions. The phase ϕ_k depends on the metal used and delivers orientational information about adsorbed species. However, defining a correct Gaussian profile together with the resonant contributions and phases can be tedious and care needs to be taken to perform reliable data analysis.

The presence of a nonresonant SFG contribution can be advantageous for alignment procedures as it is generally much stronger in comparison to the resonant contributions. The total SFG signal covers about 200 cm^{-1} in a femtosecond system. This means that broad resonant bands with widths similar to or wider than the spectral range of the IR pulse can only be detected and analyzed when the nonresonant background contribution is known. For this reason, we have included a REF beam generated prior to the sample stage (see Sec. II A), which enables reliable subtraction of nonresonant background contributions. This REF beam can also be used to normalize the spectra and, therefore, to compensate intensity drifts.

The setup described here is capable of measuring the signal and the reference beams simultaneously by recording them both on the same CCD chip. The focuses of the beams at the entrance slit are tuned with a telescope to match the f number of the spectrometer, resulting in recorded images only a few pixels in height. The reference beam is tuned to be slightly noncollinear with the signal originating from the sample allowing the separation of both signals on the CCD chip. Figure 6 shows the resulting image on the CCD.

After defining two regions of interest, one covering the sample and one the reference signal, the individual spectra are obtained by vertical binning. These spectra can then be processed in real time by a user-defined routine written for the spectrograph software (ANDOR SOLIS, v. 4.12) dividing the sample signal by the reference signal. Background-corrected SFG spectra are recorded and displayed at a rate of

up to 30 frames/s. Videos can also be obtained for analyzing dynamic processes of interest.

E. Sensitivity determination

Understanding the minimum detection capabilities of a spectroscopic system is important in determining whether or not measurements of a particular sample will be useful. In order to experimentally determine the lower detection limit of our SFG system, mixed SAMs consisting of increasingly deuterated molecules were fabricated via solution deposition and measured in the CH stretching region. Silicon wafers sputter coated with 100 nm of gold were cleaned by a UV/ozone cleaner (42–220, Jelight) for 2.5 h. The clean wafers were rinsed and placed in either pure or mixed 3 mM solutions of 1-dodecanethiol (Sigma-Aldrich) and deuterated 1-dodecanethiol (C/D/N Isotopes; 98.9% deuteration) in ethanol and incubated at room temperature for 18 h. Samples were then removed from the solutions, rinsed in ethanol, dried under flowing N_2 , and immediately measured. SFG spectra were accumulated for 1 min, analyzed according to the procedures outline in Sec. II D, and plotted without the nonresonant background contribution. The resonant SFG intensity as a function of surface coverage of the undeuterated dodecanethiol was then calculated (Fig. 7). X-ray photoelectron and IR spectroscopy measurements were also performed to ensure sample quality.

The residual peaks present in the spectrum of the fully deuterated monolayer can be assigned to CH_2 vibrations and are related to incomplete deuteration. However, the peak at 2880 cm^{-1} arising from the symmetric vibrations of the terminal CH_3 group could be used to accurately assess the SFG intensity as a function of concentration, and hence the sensitivity of the spectrometer. Note that this peak was completely absent in the fully deuterated monolayer but still present in the mixed monolayer with the lowest undeuterated content tested (4% surface coverage, corresponding to 0.19 molecules/ nm^2 assuming 0.21 nm^2 per alkanethiol molecule⁵⁴) [Fig. 7(b)]. The intensity of the SFG signal is given by

$$I_{\text{SFG}} \propto N^2 |\langle \beta \rangle|^2, \quad (7)$$

where $\langle \beta \rangle$ is the average molecular hyperpolarizability and N is the molecular surface coverage. This quadratic relationship was supported by the experimental data. Ultimately, the lower detection limit of this system was found experimentally to be 4% with a SNR of 100. Theoretically, it should be possible to achieve a signal at 2% coverage with a SNR of 25, or even at 1% coverage with a SNR of 6.25. This detection limit is lower than previously reported values for other homodyne-detected systems (10% coverage) and comparable to heterodyne-detected systems, with lower reported limits of 1% coverage.⁵¹

F. Sample cells

1. TLA cell

To study thin films on solid supports in aqueous environments, we designed a cell inspired by the IR spectroscopy cell of Skoda *et al.*⁵⁵ In this arrangement the sample is

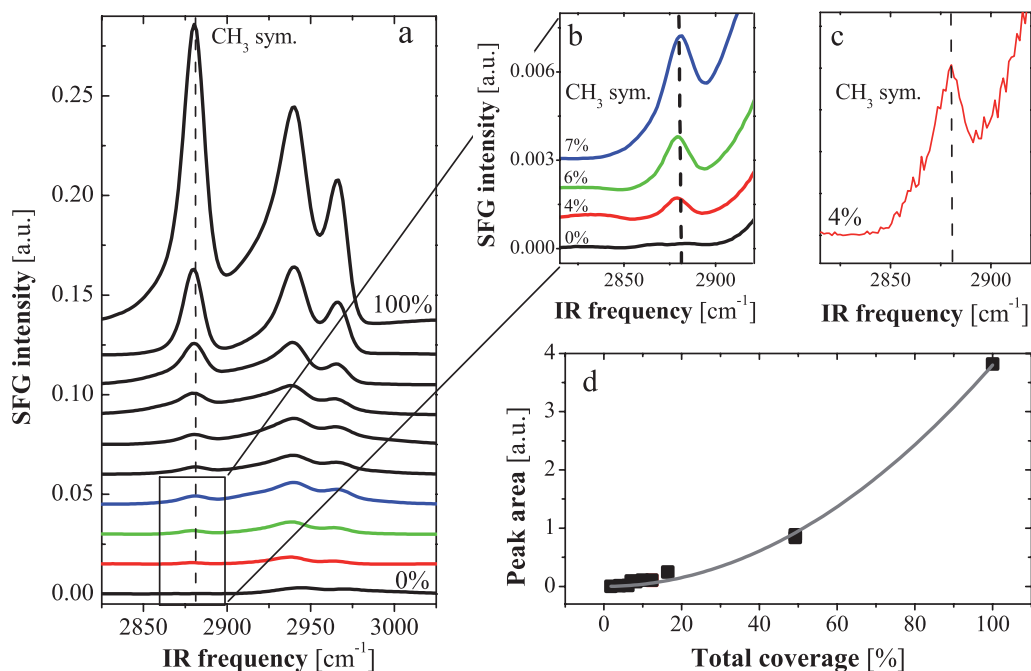


FIG. 7. (Color) Calculation of the lower detection level of the SFG system. (a) Spectra of a fully deuterated SAM (0%, bottom trace), a fully undeuterated SAM (100%, top trace), and mixtures in between (from top: 50%, 16%, 12%, 10%, 8%, 7%, 6%, and 4%). All spectra were background-subtracted, smoothed with a Savitzky–Golay routine using 15 data points, and plotted as the resonant contributions as described in Sec. II D. (b) Magnified spectra of the four lowest surface coverages highlighting the decrease in the CH₃ symmetric stretch. (c) Unsmoothed spectrum at 4% surface coverage for SNR determination. (d) Intensity of the symmetric CH₃ vibration as a function of surface coverage with the corresponding quadratic fit. The peak area was quantified using Lorentzian fits of the resonant SFG spectra.

probed through a thin aqueous layer located between it and an IR-transparent prism (Fig. 8). Overall, the TLA cell consists of five parts: (i) a base with (ii) a thermostated reservoir, (iii) a sample support, (iv) an IR-transparent prism, and (v) a vertical threaded rod fixed to a bridge for applying force to the prism.

The temperature of the TLA cell can be controlled by a thermostated bath (Ministat 230cc3, Huber). A Delrin® base holds an aluminum block which contains a serpentine cooling channel to increase the heat exchange rate. Acetal quick disconnect valved couplings (PMC series, Colder Products) allow quick mounting and unmounting without spilling cooling liquid. A kinematic mount attached to the bottom of the cell allows it to be removed and another cell put in its place as described in Sec. II C.

The support shown in Fig. 8 is designed for standard Au-coated silicon wafers; however, any kind of flat surfaces can be placed under the prism. This design allows easy exchange between different samples. It also allows the reuse of costly prisms as they do not need to be coated. For special sample shapes, the Teflon® support under the prism can be removed and replaced by other application-specific sample supports.

A hemicylindrical CaF₂ prism with optically polished curved and basal surfaces (Crystec; 13 × 20 mm) was chosen for this cell. This shape prevents reflection losses regardless of the angle, as all incoming beams are normal to the surface. Because of the curved surface, the outgoing SFG beam is slightly divergent in the incidence plane. However, the *f* number of the SFG beam can be readjusted in the

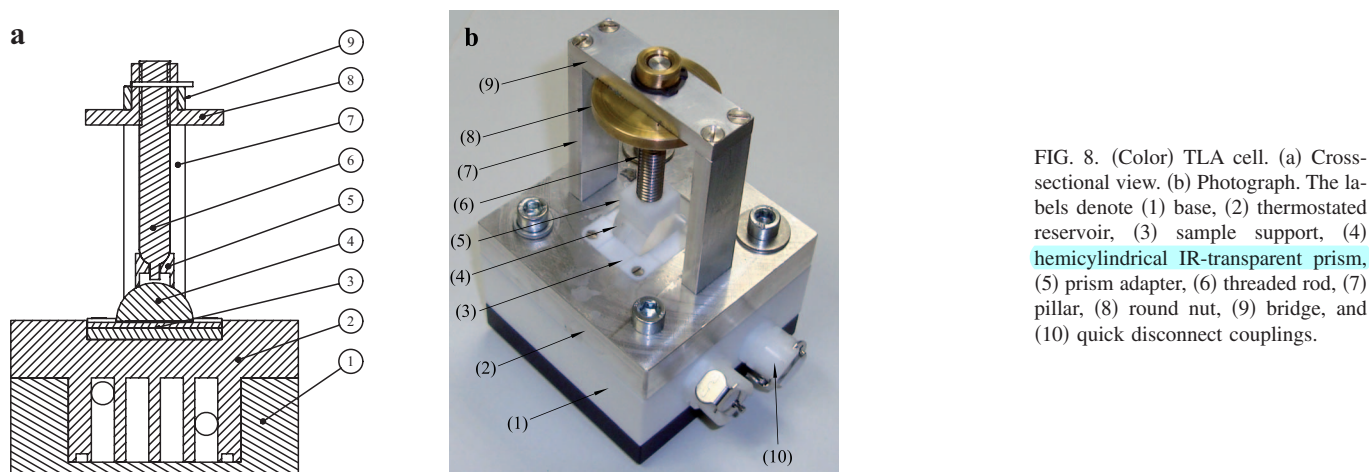


FIG. 8. (Color) TLA cell. (a) Cross-sectional view. (b) Photograph. The labels denote (1) base, (2) thermostated reservoir, (3) sample support, (4) hemicylindrical IR-transparent prism, (5) prism adapter, (6) threaded rod, (7) pillar, (8) round nut, (9) bridge, and (10) quick disconnect couplings.

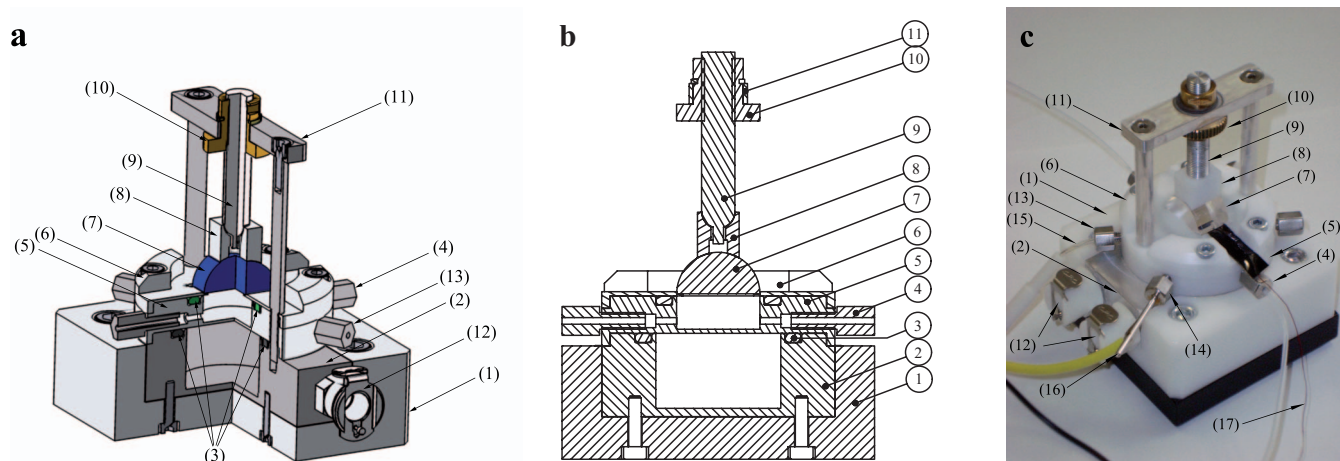


FIG. 9. (Color) SPEC cell. (a) Three-quarter view (electrodes and tubes not shown). (b) Cross-sectional view. (c) Photograph. The labels denote (1) bottom plate, (2) thermostated reservoir, (3) sealing rings, (4) solution inlet/outlet with tubes, (5) intermediary plate, (6) top plate, (7) hemicylindrical IR-transparent prism, (8) prism adapter, (9) threaded rod, (10) round nut, (11) bridge, (12) quick disconnect couplings, (13) reference electrode inlet, (14) counter electrode inlet, (15) Ag/AgCl reference electrode, (16) Pt counter electrode, and (17) Cu wire with conductive tape.

horizontal plane by the telescope in front of the vertical slit of the spectrometer. The focusing on the other axis is not crucial here since the dispersion plane of the grating is horizontal. A Teflon[®] prism adapter was fabricated to apply mechanical force to the top of the prism in order to adjust the thickness of the aqueous layer. This force can be varied by the round nut on top of the cell which drives the threaded rod into the adapter.

2. SPEC cell

In order to simultaneously make *in situ*, real-time spectroscopic, and electrochemical measurements of charged solid/liquid interfaces, we designed a measuring cell using an internal reflection configuration (Fig. 9). In this arrangement, a hemicylindrical prism with a thin conductive oxide layer coated on its basal face is brought in contact with an electrolyte solution. The surface of this prism is then probed by IR and VIS beams at incidence angles close to the TIR condition. Simultaneously, a potential difference is applied between the coated surface (which acts as a working electrode) and a counter electrode located in the solution.

This SPEC cell is composed of five parts: (i) a square-shaped bottom plate connecting the cell to the sample stage mount, (ii) a cylindrical thermostated reservoir that allows aqueous solutions to be maintained at constant temperatures, (iii) an intermediary plate acting as the aqueous reservoir with multiple ports for solution inlet/outlet, as well as counter and reference electrodes, (iv) a top plate to support the prism, and (v) an overhead bridge which holds a fine threaded rod that presses down on the prism. All parts are made of Delrin[®] acetal resin, with the exception of the thermostated reservoir and the overhead bridge which are made of stainless steel. The parts are imbricated one over the other and screwed together from the top plate side. The aqueous solution chamber and the thermostated reservoir are sealed with Viton[®] fluoropolymer sealing rings. The volume of the solution reservoir is ~ 8 ml. As was the case for the TLA cell, a hemicylindrical IR-transparent prism (CaF₂ or fused silica) was chosen. The basal face of the prism was coated

with a thin layer (~ 100 nm) of ITO (Kurt J. Lesker; 99.9995%, In₂O₃/SnO₂, 90/10 wt %) through magnetron sputtering. Amorphous sputtered ITO thin films exhibit negligible bulk nonlinear effects,⁵⁶ are relatively transparent throughout most of the near-IR region, and are also inert in most electrochemical environments.

The SPEC cell can accommodate various electrodes, sensors, and/or tubes through multiple ports positioned radially on the intermediary plate. The lateral ports are reserved for the solution inlet and outlet, while the frontal ports are used for reference and counter electrodes. The reference electrode is a commercial Ag/AgCl microelectrode (Microelectrodes) made from a Ag wire in a tube filled with saturated KCl 3M solution. A Pt wire (Metrohm) serves as the counter electrode. These electrodes are encapsulated in hollow screws that are fixed directly on the cell. The tips of both electrodes are positioned close to the center of the cell. The ITO working electrode is connected through a copper wire fixed to the base of the CaF₂ prism via a thin strip of conductive carbon adhesive tape (Plano).

III. RESULTS AND DISCUSSION

A. Spectroscopy of thin switchable polymer layers

As a demonstration of the use of the TLA cell, we studied switchable surfaces using poly(*N*-isopropylacrylamide) (pNIPAM). Before use of the cell, the prism was cleaned by UV/ozone treatment for 2.5 h followed by thorough rinsing with ethanol and acetone. The nitro-biphenyl-thiol-modified pNIPAM films were prepared by atom-transfer radical polymerization as previously described.⁵⁷ Measurements were performed by placing a drop of liquid on the sample (~ 10 – 20 μ l), gently placing the prism on top, and finally applying pressure via the nut on the bridge.

PNIPAM films undergo a temperature-driven transition in solution from a brush-like to a collapsed state around 32 °C. This is known as the lower critical solution temperature (LCST) and is accompanied by a change in wetting behavior.⁵⁸ These films are the subject of intense research

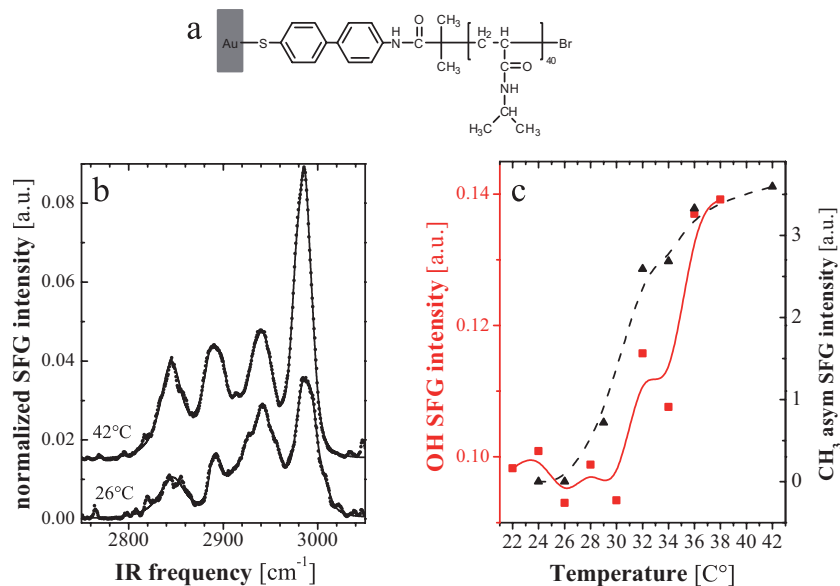


FIG. 10. (Color) (a) Chemical structure of pNIPAM. (b) SFG spectra of CH vibrations at 26 and 42 °C. (c) Integrated peak intensities of the CH₃ vibration at 2975 cm⁻¹ (black triangles and dashed line) and for the OH vibration located around 3150 cm⁻¹ (red squares and solid line).

activities in the area of biointerfaces, drug delivery systems, permeation-controlled filters, and functional composite surfaces.⁵⁹

SFG spectra of pNIPAM films in the CH stretch (2800 and 3000 cm⁻¹) below and above the LCST are depicted in Fig. 10(b). The vibration located around 2975 cm⁻¹, which is attributed to asymmetric CH₃ stretching vibration, clearly increases in intensity between 26 and 42 °C. A plot of the intensity of this peak versus temperature in small increments is shown in Fig. 10(c). Here it can be seen that the signal intensity increases around the LCST. This can be attributed to a change in orientation of the isopropyl groups [Fig. 10(a)] around this transition point.⁶⁰

In order to further study the water organization associated with these films, we have performed preliminary experiments in the OH water vibrational region around 3150 cm⁻¹. These vibrations typically reveal a broad SFG band between 3000 and 3600 cm⁻¹,^{11,12} which exceeds the 200 cm⁻¹ spectral width of the IR beam. Therefore, analysis of the SFG signal in this region requires the use of the REF beam as described in Sec. II D. Figure 10(c) shows the integrated OH peak intensity over the detected spectral region centered at 3150 cm⁻¹ (solid line). The trend observed in this region mirrors that of the CH region (dashed line).

These results demonstrate the application of the TLA cell in detecting changes in thin films at solid/liquid interfaces. This cell could also be applied to many other fields of study in surface science including investigation of biomolecules at interfaces such as DNA or peptides.^{18,61,62} Furthermore, such a device could help bridge the gap between information obtained *in vacuo* and that obtained *in situ*.

B. Spectroelectrochemistry at the ITO/water interface

In order to test the performance of the SPEC cell we measured water OH vibrations under various potentials. Before use, the cell was thoroughly cleaned in a hot Hellmanex® (Hellma) bath in order to minimize contaminants, followed by thorough rinsing with high performance liquid chromatography (HPLC) water (Sigma). The ITO sur-

face was cleaned by UV/ozone treatment in air for 1 h and rinsed thoroughly with HPLC water. The corresponding water contact angle was found to be less than 10°. HPLC water used for the experiments was deaerated by bubbling with high-purity Ar gas (99.999%) for at least 30 min prior to the SPEC measurements. The cell was slightly overfilled with water before the prism was introduced to ensure full contact between the prism and the subphase. The electrode potential was controlled with a potentiostat (Wenking LB81-M; Bank Elektronik) coupled to a voltage scanner (Wenking MVS87, Bank Elektronik). The potential scanning range was from -2 to +2 V and the scan rate was set at 40 mV/s. All potentials are given relative to Ag/AgCl.

Figure 11 shows SFG spectra in the bound-OH stretching region (3000–3500 cm⁻¹) obtained at the ITO/water interface. A SFG spectrum was taken each second and its spectral shape is a convolution of the IR beam profile and OH vibrations. Two broad peaks were observed at ~3200 and ~3400 cm⁻¹ in agreement with observations made by other groups using a similar cell configuration.^{41,46} In contrast, experiments using external reflection configurations yielded a

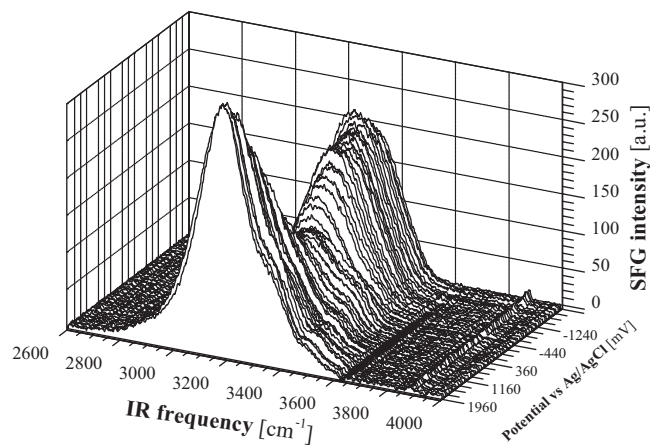


FIG. 11. SFG spectra of water in the bound-OH stretching region as function of applied voltage.

different number of peaks^{38,40} depending on the applied surface potential and electrolyte solution used.

It can be seen from Fig. 11 that the intensity changes with the applied potential and that a minimum can be found at around -320 mV. This presumably corresponds to the point of zero charge of the ITO surface. Increasing or decreasing the applied potential leads to an increased SFG response which may be related to an ordering effect of water molecules in the poling field. These preliminary data are the first SFG measurement of potential-dependent water orientation performed on a conductive metal oxide. SFG measurements in the bound-OH region were also recently obtained for NaCl and NaBr solutions. The results of these experiments will be published elsewhere.

These results demonstrate the ability of the SPEC cell to be used to investigate processes at charged interfaces. Furthermore, functionalization of the ITO layer with SAMs (Refs. 63–65) and nucleic acids⁶⁶ could allow for the study of orientation and conformation of molecular groups at the surface under various potentials, as well as the chemical tracking of electrochemical processes.

IV. CONCLUSIONS

We have presented detailed explanations and schematics for two new sample cells designed to perform SFG measurements *in situ*, as well as data demonstrating the practical use of these cells. The TLA cell was shown to be an effective platform for measurements of pNIPAM in water at incrementally increasing temperatures. With the SPEC cell, it was possible to detect the changes in orientation of water molecules at the charged ITO/water interface.

We have also described the various integrated components of our broadband SFG spectrometer optimized for measurements of solid/liquid interfaces. These include a purging chamber for working in a controlled atmosphere, a reference line for background correction and quantitative data analysis, and a flexible sample stage unit designed to accommodate multiple measuring cells. Also, details on the data analysis procedures have been discussed and the sensitivity of the system has been determined. The development and descriptions of these cells, as well as details on the SFG setup used, should facilitate future studies employing this technique at the solid/liquid interface.

ACKNOWLEDGMENTS

The authors thank M. Grunze for his support, R. Jehle and K. Schmitt (Dept. of Applied Physical Chemistry, Heidelberg University) for many useful suggestions during the engineering design work and for the machining of the measuring cells, as well as U. Liebel and M. Diesner (ITG, KIT Campus North) for help with image processing. C.H. acknowledges financial support from a U.S. NSF Graduate Research Fellowship and P. Koelsch from the Deutsche Forschungsgemeinschaft (Grant No. KO 3618-1/2).

¹B. Kasemo, *Surf. Sci.* **500**, 656 (2002).

²D. G. Castner and B. D. Ratner, *Surf. Sci.* **500**, 28 (2002).

- ³*Biomaterials Science: An Introduction to Materials in Medicine*, edited by B. Ratner, A. Hoffman, F. Schoen, and J. Lemons (Elsevier, New York, 1997).
- ⁴F. M. Geiger, *Annu. Rev. Phys. Chem.* **60**, 61 (2009).
- ⁵Y. R. Shen and V. Ostroverkhov, *Chem. Rev. (Washington, D.C.)* **106**, 1140 (2006).
- ⁶Z. Chen, Y. R. Shen, and G. A. Somorjai, *Annu. Rev. Phys. Chem.* **53**, 437 (2002).
- ⁷S. Roke, *ChemPhysChem* **10**, 1380 (2009).
- ⁸M. B. Raschke and Y. R. Shen, *Curr. Opin. Solid State Mater. Sci.* **8**, 343 (2004).
- ⁹H. C. Allen, N. N. Casillas-Ituarte, M. R. Sierra-Hernandez, X. Chen, and C. Y. Tang, *Phys. Chem. Chem. Phys.* **11**, 5538 (2009).
- ¹⁰C. S. Tian and Y. R. Shen, *Chem. Phys. Lett.* **470**, 1 (2009).
- ¹¹S. Gopalakrishnan, D. F. Liu, H. C. Allen, M. Kuo, and M. J. Shultz, *Chem. Rev.* **106**, 1155 (2006).
- ¹²G. L. Richmond, *Chem. Rev. (Washington, D.C.)* **102**, 2693 (2002).
- ¹³M. A. Leich and G. L. Richmond, *Faraday Discuss.* **129**, 1 (2005).
- ¹⁴A. J. Hopkins, C. L. McFearin, and G. L. Richmond, *Curr. Opin. Solid State Mater. Sci.* **9**, 19 (2005).
- ¹⁵J. Kim, G. Kim, and P. S. Cremer, *J. Am. Chem. Soc.* **124**, 8751 (2002).
- ¹⁶V. Ostroverkhov, G. A. Waychunas, and Y. R. Shen, *Chem. Phys. Lett.* **386**, 144 (2004).
- ¹⁷M. A. Even, C. Chen, J. Wang, and Z. Chen, *Macromolecules* **39**, 9396 (2006).
- ¹⁸O. M. Mermut, D. C. Philips, R. L. York, K. R. McCrea, R. S. Ward, and G. A. Somorjai, *J. Am. Chem. Soc.* **128**, 3598 (2006).
- ¹⁹P. L. Hayes, E. H. Chen, J. L. Achtyl, and F. M. Geiger, *J. Phys. Chem. A* **113**, 4269 (2009).
- ²⁰P. T. Wilson, L. J. Richter, W. E. Wallace, K. A. Briggman, and J. C. Stephenson, *Chem. Phys. Lett.* **363**, 161 (2002).
- ²¹R. L. York, Y. Li, G. J. Holinga, and G. A. Somorjai, *J. Phys. Chem. A* **113**, 2768 (2009).
- ²²K. A. Becraft and G. L. Richmond, *Langmuir* **17**, 7721 (2001).
- ²³P. L. Hayes, J. N. Malin, C. T. Konek, and F. M. Geiger, *J. Phys. Chem. A* **112**, 660 (2008).
- ²⁴M. J. Stein, T. Weidner, K. McCrea, D. G. Castner, and B. D. Ratner, *J. Phys. Chem. B* **113**, 11550 (2009).
- ²⁵N. Nishi, D. Hobara, M. Yamamoto, and T. Kakiuchi, *Anal. Sci.* **19**, 887 (2003).
- ²⁶Y. Nishikawa, T. Nagasawa, and K. Fujiwara, *Vib. Spectrosc.* **6**, 43 (1993).
- ²⁷A. Tadjeddine and F. Vidal, *In-Situ Spectroscopic Studies of Adsorption at the Electrode and Electrocatalysis* (Elsevier, New York, 2007) Chap. 9, pp. 273–298.
- ²⁸P. Guyot-Sionnest and A. Tadjeddine, *Chem. Phys. Lett.* **172**, 341 (1990).
- ²⁹A. Peremans, A. Tadjeddine, and P. Guyot-Sionnest, *Chem. Phys. Lett.* **247**, 243 (1995).
- ³⁰S. Baldelli, N. Markovic, P. Ross, Y.-R. Shen, and G. Somorjai, *J. Phys. Chem. B* **103**, 8920 (1999).
- ³¹F. Dederichs, K. A. Friedrich, and W. Daum, *J. Phys. Chem. B* **104**, 6626 (2000).
- ³²A. Tadjeddine and P. Guyot-Sionnest, *Electrochim. Acta* **36**, 1849 (1991).
- ³³T. H. Ong, P. B. Davies, and C. D. Bain, *J. Phys. Chem.* **97**, 12047 (1993).
- ³⁴F. Huerta, E. Morralo, C. Quijada, J. L. Vázquez, and A. Aldaz, *Electrochim. Acta* **44**, 943 (1998).
- ³⁵B. Bozzini, C. Mele, A. Fanigliulo, B. Busson, F. Vidal, and A. Tadjeddine, *J. Electroanal. Chem.* **574**, 85 (2004).
- ³⁶M. Tadjeddine, J.-P. Flament, A. L. Rille, and A. Tadjeddine, *Surf. Sci.* **600**, 2138 (2006).
- ³⁷W. Q. Zheng, O. Pluchery, and A. Tadjeddine, *Surf. Sci.* **502–503**, 490 (2002).
- ³⁸W. Zheng and A. Tadjeddine, *J. Chem. Phys.* **119**, 13096 (2003).
- ³⁹S. Nihonyanagi, S. Ye, K. Uosaki, L. Dreesen, C. Humbert, P. Thiry, and A. Peremans, *Surf. Sci.* **573**, 11 (2004).
- ⁴⁰Z. D. Schultz, S. K. Shaw, and A. A. Gewirth, *J. Am. Chem. Soc.* **127**, 15916 (2005).
- ⁴¹H. Noguchi, T. Okada, and K. Uosaki, *Faraday Discuss.* **140**, 125 (2009).
- ⁴²M. A. Hines, J. A. Todd, and P. Guyot-Sionnest, *Langmuir* **11**, 493 (1995).
- ⁴³J. Hedberg, C. Leygraf, K. Cimat, and S. Baldelli, *J. Phys. Chem. C* **111**, 17587 (2007).
- ⁴⁴D. Qu, B.-C. Kim, and C.-W. J. Lee, *J. Phys. Chem. C* **114**, 497 (2010).
- ⁴⁵D. S. Bethune, A. C. Luntz, J. K. Sass, and D. K. Roe, *Surf. Sci.* **197**, 44 (1988).

- ⁴⁶H. Noguchi, T. Okada, and K. Uosaki, *Electrochim. Acta* **53**, 6841 (2008).
- ⁴⁷H. Asanuma, H. Noguchi, K. Uosaki, and H.-Z. Yu, *J. Phys. Chem. C* **113**, 21155 (2009).
- ⁴⁸F. Vidal and A. Tadjeddine, *Rep. Prog. Phys.* **68**, 1095 (2005).
- ⁴⁹T. Weidner, N. T. Samuela, K. McCrea, L. J. Gamble, R. S. Ward, and D. G. Castner, *Biointerphases* **5**, 9 (2010).
- ⁵⁰L. J. Richter, T. P. Petralli-Mallow, and J. C. Stephenson, *Opt. Lett.* **23**, 1594 (1998).
- ⁵¹I. V. Stiopkin, H. D. Jayathilake, A. N. Bordenyuk, and A. V. Benderskii, *J. Am. Chem. Soc.* **130**, 2271 (2008).
- ⁵²C. D. Bain, *J. Chem. Soc., Faraday Trans.* **91**, 1281 (1995).
- ⁵³L. Dreesen, C. Humbert, M. Celebi, J. J. Lemaire, A. A. Mani, P. A. Thiry, and A. Peremans, *Appl. Phys. B: Lasers Opt.* **74**, 621 (2002).
- ⁵⁴R. Maoz, J. Sagiv, D. Degenhardt, H. Möhwald, and P. Quint, *Supramol. Sci.* **2**, 9 (1995).
- ⁵⁵M. Skoda, R. Jacobs, S. Zorn, and F. Schreiber, *J. Electron Spectrosc. Relat. Phenom.* **172**, 21 (2009).
- ⁵⁶W. Wang, J. Xu, X. Liu, Y. Jiang, G. Wang, and X. Lu, *Thin Solid Films* **365**, 116 (2000).
- ⁵⁷S. Schilp, N. Ballav, and M. Zharnikov, *Angew. Chem., Int. Ed.* **47**, 6786 (2008).
- ⁵⁸X. Cheng, H. E. Canavan, M. J. Stein, J. R. Hull, S. J. Kweskin, M. S. Wagner, G. A. Somorjai, D. G. Castner, and B. D. Ratner, *Langmuir* **21**, 7833 (2005).
- ⁵⁹M. A. Cole, N. H. Voelcker, H. Thissen, and H. J. Griesser, *Biomaterials* **30**, 1827 (2009).
- ⁶⁰V. Kurz, M. Grunze, and P. Koelsch, *ChemPhysChem* **11**, 1425 (2010).
- ⁶¹C. Howell, R. Schmidt, V. Kurz, and P. Koelsch, *Biointerphases* **3**, FC47 (2008).
- ⁶²S. R. Walter and F. M. Geiger, *J. Phys. Chem.* **1**, 9 (2010).
- ⁶³C. Yan, M. Zharnikov, A. Götzhäuser, and M. Grunze, *Langmuir* **16**, 6208 (2000).
- ⁶⁴N. Karsi, P. Lang, M. Chehimi, M. Delamar, and G. Horowitz, *Langmuir* **22**, 3118 (2006).
- ⁶⁵V. M. Bermudez, A. D. Berry, H. Kim, and A. Piqué, *Langmuir* **22**, 11113 (2006).
- ⁶⁶P. M. Armistead and H. H. Thorp, *Anal. Chem.* **72**, 3764 (2000).